JACS
JOURNAL OF THE AMERICAN CHEMICAL SOCIETY
Article
pubs.acs.org/JACS

Quantitative Correlation between Defect Density and Heterogeneous Electron Transfer Rate of Single Layer Graphene

Jin-Hui Zhong,[†,§] Jie Zhang,[†,§] Xi Jin,[†] Jun-Yang Liu,[†] Qiongyu Li,[‡] Mao-Hua Li,[†] Weiwei Cai,[†,‡] De-Yin Wu,[†] Dongping Zhan,*[,†] and Bin Ren*[,†]

[†]State Key Laboratory of Physical Chemistry of Solid Surfaces, Collaborative Innovation Center of Chemistry for Energy Materials, the MOE Key Laboratory of Spectrochemical Analysis & Instrumentation, and Department of Chemistry, College of Chemistry and Chemical Engineering, and [‡]Department of Physics, Laboratory of Nanoscale Condensed Matter Physics, Xiamen University, Xiamen 361005, China

S Supporting Information

ABSTRACT: Improving electrochemical activity of graphene is crucial for its various applications, which requires delicate control over its geometric and electronic structures. We demonstrate that precise control of the density of vacancy defects, introduced by Ar^+ irradiation, can improve and finely tune the heterogeneous electron transfer (HET) rate of graphene. For reliable comparisons, we made patterns with different defect densities on a same single layer graphene sheet, which allows us to correlate defect density (via Raman spectroscopy) with HET rate (via scanning electrochemical microscopy) of graphene quantitatively, under exactly the same experimental conditions. By balancing the defect induced increase of density of states (DOS) and decrease of conductivity, the optimal HET rate is attained at a moderate defect density, which is in a critical state; that is, the whole graphene sheet becomes electronically activated and, meanwhile, maintains structural integrity. The improved electrochemical activity can be understood by a high DOS near the Fermi level of defective graphene, as revealed by ab initio simulation, which enlarges the overlap between the electronic states of graphene and the redox couple. The results are valuable to promote the performance of graphene-based electrochemical devices. Furthermore, our findings may serve as a guide to tailor the structure and properties of graphene and other ultrathin two-dimensional materials through defect density engineering.

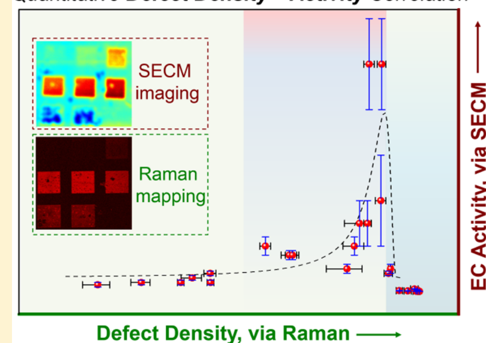

1. INTRODUCTION

The rational control of the structural, electronic, and chemical properties of graphene is an important issue for its dedicated applications. As a new type of carbon electrode, graphene provides opportunities to understand the fundamental electrochemistry of a single atomic carbon layer.[1−5] It also shows great potential for application in capacitance[6] and electrocatalysis.[7−9] As for electrocatalysis, the performance of graphene is still not comparable with Pt-based catalysts and requires further improvement. The performance of graphene relies strongly on its geometric and electronic structures. Great efforts have been made on structural modifications to improve its performance.[10,11] Defects in graphene,[12] especially the point defects, have been found to be capable of modifying the local atomic structure and tailoring its mechanical,[13] electronic,[14] magnetic,[15] and plasmonic[16] properties. We demonstrate here that precise control of the density of vacancy defect allows a fine-tuning of the electrochemical activity of graphene.

In electrochemistry, the edge plane were consider to be much more reactive than the basal plane for graphite-based electrodes.[17−24] However, recent studies by scanning electrochemical (cell) microscopy (SEC(C)M) with high spatial resolution revealed that there is no apparent difference between the basal and edge plane sites of graphite and carbon nanotubes.[25−27] The activity of basal plane depended on the history and electrochemical cycling of the surface.[25,26] With respect to graphene, its basal plane was reported to allow fast heterogeneous electron transfer (HET).[1] Nonetheless, the edge plane of graphene showed much higher electron transfer rates, and better capacitive and electrocatalytic performance than the basal plane.[24,28−30] Nanoscale reduced graphene oxide showed high electron transfer rate because of the abundant defect and edge site structure.[31] Although these reports demonstrate the significant effect of defects on the electrochemical performance of graphene, the edge plane sites are difficult to be controlled and quantified. Additionally, it is not sufficient to utilize only the edge plane sites due to the low edge/basal plane ratio in the two-dimensional structure of graphene. Therefore, it is critical to maximize the carbon utilization in the basal plane of graphene. Zero-dimensional point defects, especially vacancy defects that could be readily introduced in the basal plane by ion or electron irradiation, are promising because of the well-defined structure and good controllability.[15,32−37] That means

Received: August 30, 2014
Published: October 28, 2014

 © 2014 American Chemical Society

point defects in the basal plane hold greater potential than edge plane sites in fully exploiting the potential of graphene. Unfortunately, the influence of point defects on the electrochemical properties of graphene, as well as the methodology for the rational control of defect density to optimize its performance, remain incompletely understood.

Most studies on the effect of defect or edge plane density of graphite electrode were made by comparing different ensemble electrodes or the same electrodes with different treatments,[17,18,23,24] which hampers a direct comparison, because the chemical and physical properties of graphite and graphene surface are sensitive to the fabrication method and pretreatment procedures. In addition, to make it suitable for electrochemical system, the single layer graphene has to go through more complicated fabrication processes. As a result, different batches of graphene samples may vary significantly in surface properties, making it rather difficult to study the effect of defect on the electrochemical activities.

Herein, we investigate the influence of defect density on the electrochemical activity of single layer graphene by SECM and Raman spectroscopy in combination with ab initio simulation. To make reliable comparisons, we employ a lithography approach to fabricate patterns with different defect densities on the same single layer graphene sheet. The defects were introduced by Ar^+ irradiation, and the defect density was finely tuned by the ion dose irradiated at different regions on graphene. We adopted Raman spectroscopy to determine the defect density,[36−38] because it is a well-established technique for probing various properties of graphene.[39,40] The Raman-forbidden D and D′ peaks in pristine graphene can be activated by structural defects. A quantitative relationship between the defect density and the intensity ratio of I_D/I_G has been reported recently, which allows one to readily determine the defect density by Raman spectroscopy.[36] The SECM technique, utilizing an ultramicroelectrode (UME), is able to measure electron transfer kinetics and image local electrochemical activities. The combination of SECM with Raman spectroscopy allows us to investigate the correlation between defect density and electrochemical activity of graphene in a well-controlled way. The optimal electrochemical activity is achieved by balancing the defect induced increase of density of states (DOS) and decrease of conductivity. The improved electrochemical activity can be understood by a high DOS near the Fermi level of graphene in the vicinity of a point defect, thus, a larger overlap between the electronic states of graphene and the redox couple, as revealed by ab initio simulation. The results suggest that rational control of the defect density for tuning electrochemical activity of graphene will lead to better performance of graphene-based electrochemical devices.

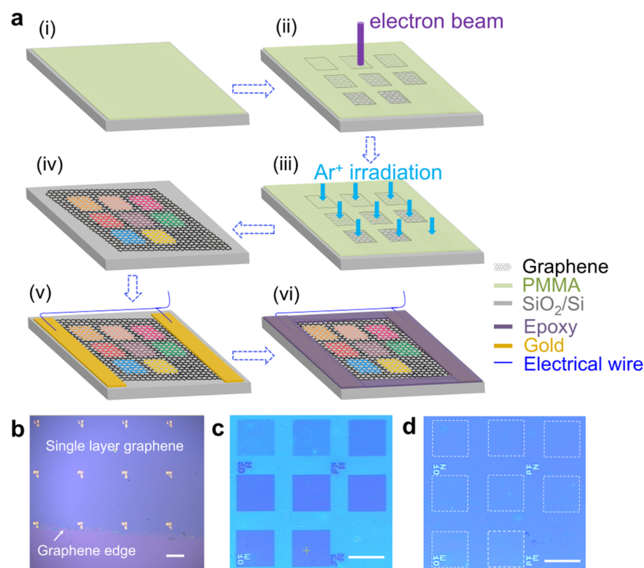

Figure 1. (a) Fabrication of defective graphene patterns. (i) 100 nm-thick PMMA was coated on single layer graphene as protection layer. (ii) The PMMA protection layer was patterned with different thickness by EBL. (iii) The whole sample was exposed to Ar^+ irradiation to produce defective graphene patterns with various defect densities. (iv) The PMMA protection layer was removed by acetone and chloroform. Different colors represent different defect densities. (v) The gold connector was deposited on both ends of graphene, which was connected to external circuit by electrical wires. (vi) The sample was sealed to leave the graphene basal plane with defective patterns. (b) An optical image of a single layer graphene sheet on a 300 nm SiO_2/Si substrate. Optical images of the defective graphene patterns after Ar^+ irradiation (c) and fabricated as an electrode (d). In (d), the boundaries of the defective graphene patterns are marked by a dashed rectangle. Scale bars in (b), (c), and (d) indicate 100 μm.

2. EXPERIMENTAL SECTION

Graphene Sample and Defect Engineering. Single layer graphene was prepared by chemical vapor deposition (CVD)[41] and transferred to a 300 nm SiO_2/Si substrate using poly(methyl methacrylate) (PMMA) as a transfer mediator.[42] For fabricating defective graphene patterns, a layer of 100 nm PMMA (950 K) was spin-coated on the top of graphene, and standard electron beam lithography (EBL) was employed to expose different electron dose in different patterns (100 × 100 μm^2 area, Figure 1). The exposure of PMMA to an electron beam leads to the fracture and scission of the polymer chains, which becomes more soluble in the chemical developer. Therefore, a longer exposure time to electron beam resulted in a thinner PMMA layer. Meanwhile, the thickness of the PMMA in the untreated area remains unchanged. The graphene sample was then treated with Ar^+ plasma to introduce vacancy defects. The plasma treatments were carried out at a pressure of 0.6 Torr of Ar gas and a power of 6.8 W using inductively coupled plasma at radio frequency of 13.56 MHz. The low power can avoid rapid damage of the sample. The treatment duration was 5−10 min. The PMMA was removed by acetone and chloroform. The samples were then annealed at 250 °C under H_2 atmosphere for 1 h to remove any possible residuals remaining on the surface of graphene. Thus, a graphene sample with well-defined defect patterns was prepared. A 300 nm gold layer was deposited on both ends of the single layer graphene sheet to contact with the external circuit. Finally, the graphene edges and the electrical contacts were covered with epoxy, while the basal plane with pristine graphene and defective graphene patterns was exposed for further experiments.[3]

Raman, XPS, and AFM Characterization. All of the Raman measurements were performed with 532 nm laser excitation. Raman mapping was performed on Nanophoton (laser Raman microscope RAMAN-11) in a fast line scanning mode with a 20× objective (NA = 0.45) and 600 lines/mm grating. To gain better spectral resolution, single spot Raman spectra were measured on Xplora (Horiba Jobin Yvon, France) with 1200 lines/mm grating. The laser power was kept at 1 mW with typical acquisition time of 5 s. The laser spot size is about 2 μm using a 50× objective (NA = 0.55). About 10 Raman spectra were acquired for each defective pattern. The Raman spectra were fitted by Gaussian−Lorentzian function to extract the relevant parameters, including the frequency, bandwidth, and intensity of the D, G, D′, and 2D bands of graphene. The intensity of peak height was used to deduce the defect density.[36−38] X-ray photoelectron spectroscopy (XPS) measurements were carried out on an Omicron Sphera II hemispherical electron energy analyzer (Monochromatic Al K_α with 1486.6 eV operating at 15 kV and 300 W). The base pressure

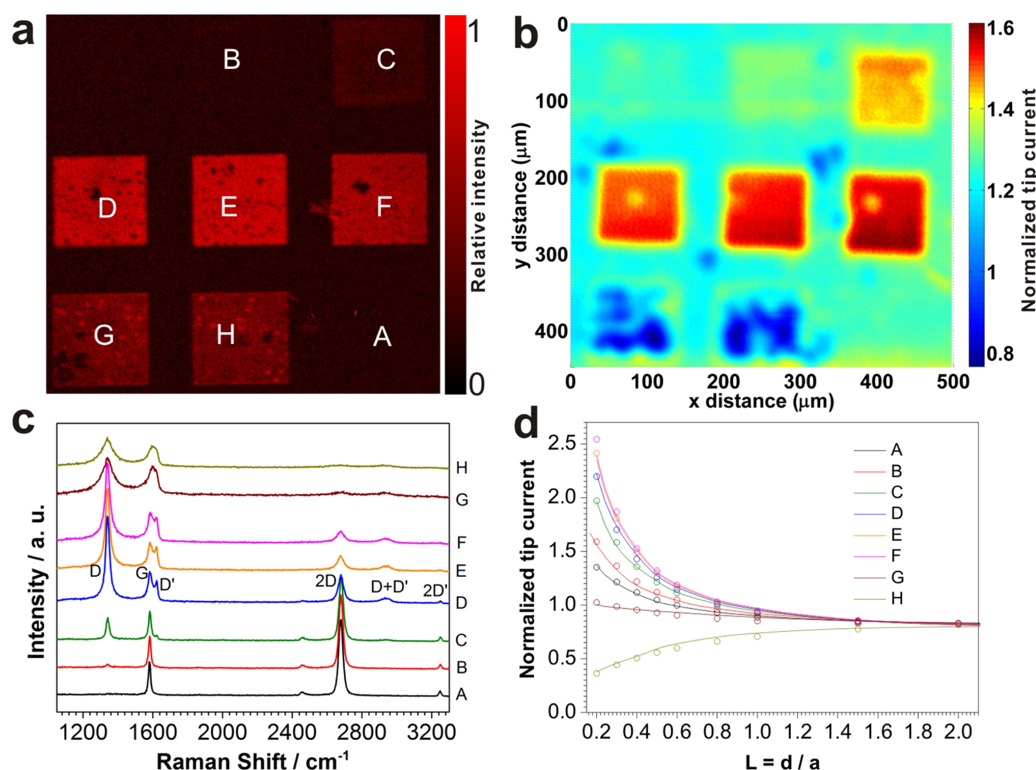

Figure 2. (a) Raman mapping of the D band of the defective graphene patterns. The optical picture of the sample is shown in Figure 1d. (b) SECM images of the same defective graphene patterns with a tip potential of 0.4 V and a substrate potential of 0.11 V. The tip−substrate distance was kept constant at 8 μm (d/a = 0.67). (c) The corresponding Raman spectra (vertically aligned) and (d) SECM approach curves obtained on each defective graphene pattern, with a tip potential of 0.4 V and a substrate potential of 0.18 V.

of the systems was 5.0×10^{-9} mbar. Atomic force microscopy (AFM) was performed on a NT-MDT system (NTEGRA Spectra) in tapping mode. Typical images with $10 \times 10\ \mu m^2$ area were obtained at a scan rate of 0.5 Hz using VIT_P tip.

SECM Characterization. All of the electrochemical measurements were performed with a CHI 920c workstation (CH Instruments Inc.). A 12.5-μm radius (r) Pt UME (RG = 2) and the above-mentioned single layer graphene electrode were used as the SECM tip and substrate, respectively. The tip was polished by using alumina (particle size: 0.3 μm) slurry and sonicated in ultrapure water (Milli-Q) before experiments. A Pt wire and an Ag/AgCl electrode were used as the counter electrode (CE) and reference electrode (RE), respectively. All of the potential referred to in this Article is relative to the Ag/AgCl electrode. The tip−substrate distance was determined by the positive approach curves obtained with an aqueous solution containing 1 mM hydroxymethylferrocene (FcMeOH) and 0.1 M KCl. During the positioning experiment, the tip potential was held at 0.4 V, while the potential of the graphene substrate was held at 0 V to ensure the purely diffusion-controlled condition. In the SECM imaging experiment, the tip was biased at 0.4 V and the potential of the graphene substrate was at open circuit potential (0.11 V). After each imaging operation, approaching curve was recorded on each defective pattern with a tip potential of 0.4 V and a substrate potential of 0.18 V (close to the formal potential).

Finite Element Method (FEM) Modeling. The electrochemical kinetics of the single layer graphene with different defect densities were derived by solving the time-dependent mass transport equations with a software package of COMSOL Multiphysics 4.3b (COMSOL AB, Sweden). The details including the axisymmetric cylindrical coordinates, geometry of the model, and the boundary conditions are provided in the Supporting Information; see section S3, equations S3−6, Figures S7−9, and Table S1.

Ab Initio Simulation. Both the pristine and the defective single layer graphene were simulated by a slab model with a vacuum layer of 15 Å. Theoretical calculations based on density functional theory are performed with the Perdew−Burke−Ernzerhof generalized-gradient approximation (GGA-PBE)[43] exchange-correlation functional, as implemented in the Quantum ESPRESSO package.[44] The projector augmented wave (PAW) method[45] was applied. The kinetic energy cutoff for wave function was tested carefully and set to be 40 Ry. Spin-polarization was examined for all structures and was not taken into account in calculating the DOS when it was negligible. The lattice constant of pristine graphene was set to be 2.46 Å. The Monkhorst−Pack approach[46] of k-point sampling is applied with grids of $9 \times 9 \times 1$ and $7 \times 7 \times 1$ for two-dimensional supercells of 3×3 and 5×5 in sizes, respectively. In the DOS calculations, sufficiently dense k-point sampling was applied to smooth the DOS curve. The convergence threshold on forces for all geometric structure optimization was set to be 1.0×10^{-3} au.

3. RESULTS AND DISCUSSION

Control of Different Defect Densities on the Same Single Layer Graphene Sheet. HET processes are fundamentally important for the surface and interfacial electron transfer reactions on graphene. Here, we study the influence of defect and defect density on the HET rate and optimized defect density of graphene for the best electrochemical activity. To this end, we introduced point vacancy defects controllably on single layer graphene by Ar^+ irradiation. Electron and ion irradiation have been found to introduce defects on carbon nanotube and graphene in an efficient and controllable manner.[32,33,35] Theoretical[47] and experimental[35,48] results have demonstrated that Ar^+ irradiation induces mono- and divacancy defects on graphene by knock-on displacement of carbon atoms. The defect density is tunable by the irradiation time and ion dose.

Figure 1b shows an optical image of the pristine single layer graphene on SiO_2/Si substrate. A series of defect densities were

Table 1. Summary of the Defect Density and the Corresponding Electron Transfer Kinetics of the Sample Shown in Figure 2

regions	I_D/I_G [a]	L_D (nm) [a]	n_D (cm^{-2}) [a]	k^0 (cm/s) [b]
A				$(1.0 \pm 0.2) \times 10^{-2}$
B	0.15 ± 0.03	27.96 ± 3.60	$(4.20 \pm 1.02) \times 10^{10}$	$(1.5 \pm 0.5) \times 10^{-2}$
C	0.75 ± 0.13	11.78 ± 1.20	$(2.35 \pm 0.43) \times 10^{11}$	$(3.0 \pm 0.5) \times 10^{-2}$
D	2.95 ± 0.17	3.00 ± 0.71	$(3.92 \pm 1.23) \times 10^{12}$	$(5.0 \pm 1.0) \times 10^{-2}$
E	2.94 ± 0.16	2.70 ± 0.29	$(4.48 \pm 0.84) \times 10^{12}$	$(1.0 \pm 0.2) \times 10^{-1}$
F	2.65 ± 0.09	2.36 ± 0.08	$(5.70 \pm 0.38) \times 10^{12}$	$(1.5 \pm 0.5) \times 10^{-1}$
G	1.31 ± 0.07	1.54 ± 0.05	$(1.34 \pm 0.09) \times 10^{13}$	$(5.5 \pm 0.5) \times 10^{-3}$
H	1.22 ± 0.05	1.52 ± 0.04	$(1.38 \pm 0.08) \times 10^{13}$	$(5.5 \pm 2.0) \times 10^{-4}$

[a]Errors represent the standard deviation in deducing the defect density of graphene using 10 Raman spectra measured for each defective graphene pattern. [b]Errors represent the uncertainty in fitting k^0.

introduced on the same graphene sheet. This design allows one to avoid the influence of different fabrication and pretreatment procedure on the surface properties of graphene. It also allows one to fast obtain systematic defect density correlated electrochemical activity of graphene by simply imaging the sample surface. For this purpose, a layer of 100 nm PMMA was first coated on the top of graphene sheet as a protective layer (Figure 1a,i). EBL was employed to adjust the PMMA thickness on different patterns by tuning the illuminated electron dose (Figure 1a,ii). Several sets of such patterns were made to have a wide range of defect densities on the same graphene sheet. The graphene sheet was then irradiated by Ar^+ plasma, while the PMMA layer acts as the barrier of irradiation. Only when the top PMMA was completely etched could the underneath graphene be irradiated (Figure 1a,iii, c). Thereby, the thickness of the PMMA above graphene determines the effective ion dose and, consequently, the defect density on different patterns. After removing PMMA by acetone and chloroform (Figure 1a,iv), the sample was annealed under H_2 atmosphere to remove any residuals. A 300 nm thick gold was then deposited on both ends of graphene, which served as the contacts to external circuit (Figure 1a,v). The gold and graphene edges were then covered by epoxy (Figure 1a,vi).[3]

This fabrication method allows for tuning defect density in the range from 10^{11} to $10^{14}/cm^2$ on different patterns of the same graphene sheet (the intrinsic atom density of pristine graphene is about $3.82 \times 10^{15}/cm^2$). Therefore, our graphene electrode is suited for studying the correlation between defect density and electrochemical activity of graphene.

Quantification of the Defect Densities. Raman spectroscopy was applied to quantify the defect density of our graphene sample, and the results are shown in Figure 2c, which are in agreement with literature reports.[39,40] The G band at ~1580 cm^{-1} corresponds to the E_{2g} phonon at the Brillouin zone center. The D (~1345 cm^{-1}) and D′ (~1620 cm^{-1}) peaks appear only in defective graphene, and are the characteristics of defects.[39,40] Other features in the Raman spectra are the second-order 2D (~2680 cm^{-1}) and 2D′ (~3247 cm^{-1}) peaks, and the combination mode of D and D′ (~2940 cm^{-1}).[40] For the pristine graphene, the 2D peak is symmetric and its intensity is much stronger than that of the G peak, indicating the graphene is single layer (spectrum A in Figure 2c). The absence of the D peak confirms that the graphene is defect free.

Recently, extensive efforts have been made to study the relationship between the amount and nature of defects and the intensity of the D and D′ peaks.[36−38,49,50] A quantitative formula has been proposed to correlate the mean distance between defects in graphene (L_D, nm) with the intensity ratio of I_D/I_G:

$$\frac{I_D}{I_G} = C_A \frac{(r_A^2 - r_S^2)}{(r_A^2 - 2r_S^2)} \left[e^{-\pi r_S^2/L_D^2} - e^{-\pi (r_A^2 - r_S^2)/L_D^2} \right] \quad (1)$$

where r_S (1 nm) and r_A (3.1 nm) are the radii of the "structurally disordered" area and the "activated" area around the ion-induced defects, respectively.[36] The factor C_A is defined by the electron−phonon matrix elements.[36] We used $C_A = 4.2$ at the green line excitation (see Supporting Information section S1 and Figure S1 for details).[36] The defect density n_D (cm^{-2}) is then given by $n_D = 10^{14}/\pi L_D^2$.[37] Both L_D and n_D have been used to quantify the defect density in graphene.

Figure 2a presents the Raman mapping of the D band, showing the well-defined defective patterns (Figure 1c). We named the different patterns from A to H for convenience of discussion (Figure 2a), where region A is the pristine graphene. The Raman mapping of the G and 2D bands also displays similar patterns (Supporting Information Figure S2). The pristine graphene is dark in Figure 2a due to the absence of the D band. The intensity of the D band varies from pattern to pattern, which indicates the varying defect densities. This is further evidenced by the Raman spectra depicted in Figure 2c. In the defective patterns, the D peak appears, with intensity increasing from pattern B to E followed by an intensity decreasing and spectral broadening from pattern F to H. This two-stage spectral change is typically observed when increasing the defect density in graphene.[36−38] At low defect density, the defects are separated and independent. The increasing "activated" area would result in a stronger D band until the intensity reaches a maximum (stage 1, Supporting Information Figure S3). With further increasing the defect density, the "activated" area starts to coalesce and the "structurally disordered" area would be dominated in the graphene sheet, which leads to the decrease of the D band intensity (stage 2, Supporting Information Figure S3).[36−38] Hence, a given value of I_D/I_G may correspond to two possible L_D values. The two stages could be discriminated by the peak width of the D, G, D′, and 2D bands.[38] In stage 2, all of these peaks start to broaden significantly (Supporting Information Figure S3b). Therefore, we are able to deduce the defect density from I_D/I_G by using eq 1, and the results are summarized in Table 1. The Raman results indicate that we have succeeded in controlling different defect densities on the same single layer graphene sheet.

Determination of the HET Rates at Defective Graphene Patterns. Feedback modes of SECM were employed to study the electrochemical activity of defective graphene, in which an oxidized species on the tip is reduced (regenerated) by the graphene substrate (see Supporting Information Figure S4 for the scheme of SECM). The feedback

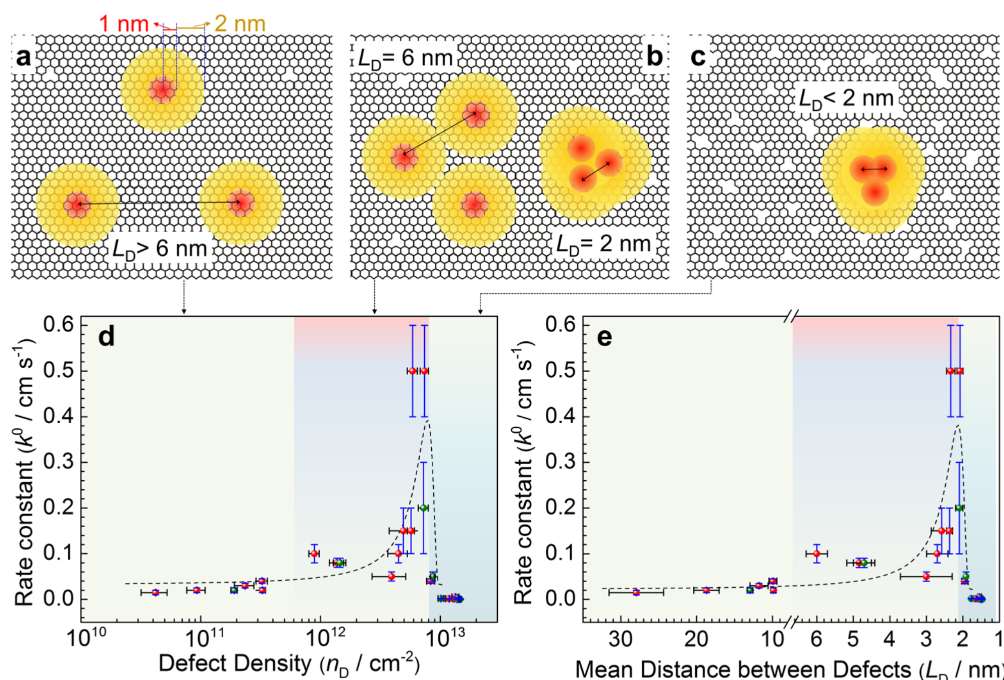

Figure 3. Defect density correlated HET rate of graphene. The microscopic model in different defect density ranges: (a) low defect density with $L_D > 6$ nm; (b) moderate defect density with 2 nm $\leq L_D \leq$ 6 nm; (c) high defect density with $L_D < 2$ nm. The area in red is the structurally disordered area with a radius of 1 nm; the area in yellow is the electronically activated but structurally preserved area (1 nm < r < 3 nm). The standard HET rate constant k^0 as a function of defect density n_D (cm^{-2}) (d) and the mean distance between defects L_D (nm) (e). The dashed lines in (d) and (e) are a guide for the eye only. The vertical error bar in (d) and (e) represents the uncertainty in fitting k^0. The horizontal error bar is the standard deviation in deducing the defect density n_D or the mean distance between defects from 10 Raman spectra measured for each defective pattern.

current of the tip is dependent on the HET capability of the local area on graphene. The FcMeOH was used as the redox couple because the outer-sphere reaction involves no specific surface interaction between FcMeOH and graphene (and defects). A typical cyclic voltammogram (CV) of a pristine graphene electrode in the FcMeOH solution is shown in Supporting Information Figure S5. The CV indicates quasi-reversible electrochemical kinetics of FcMeOH on our CVD graphene, in accordance with the literature[1] and our previous study.[3] A Pt UME (radius of 12.5 μm) with RG = 2 (see Supporting Information section S2 for details) was adopted as the SECM tip. The potential of the Pt tip was held at E_T = 0.4 V to ensure the oxidation of FcMeOH under a diffusion-limited condition. The potential of the graphene substrate (E_G) was at 0.11 V to reduce the $FcMeOH^+$ species generated at the tip.

Figure 2b presents the SECM image of the graphene sample shown in Figures 1d and 2a. It is observed clearly that the normalized feedback currents above the defective patterns are different from each other and also that above pristine graphene, indicating that the electrochemical activities of graphene depend on the defect density. The higher is the feedback current, the faster is the local HET rate. Figure 2b shows that with increasing defect density, the tip current first increases (from pattern B to F) and then decreases (pattern G to H) to even below that of the pristine graphene. The two-stage SECM images are in accordance with the Raman D-band mapping results, suggesting the defect density-dependent electrochemical activity of single layer graphene. Additional Raman and SECM results on other sets of defective graphene patterns are provided in Supporting Information Figure S6, which also show a good correlation between them.

To quantify the HET rate, the approaching curves were measured above the defective graphene patterns with different defect densities. The potentials of the Pt tip and the graphene substrate were kept at 0.4 and 0.18 V, respectively. As shown in Figure 2d, when $L = d/a \leq 1$, the normalized feedback current increases gradually with increasing defect density (pattern B to F), and then decreases in the higher defect density regions (pattern G to H). The results are in harmonious accordance with the SECM images. FEM modeling was used to simulate the tip current response as a function of the standard HET rate constant, k^0, through COMSOL Multiphysics 4.3b (details are provided in Supporting Information section S3, Figures S7 and S8, and Table S1). The transfer coefficient (α) is assumed to be 0.5 in the kinetic studies with the Butler−Volmer model (Supporting Information eqs S3 and S4) on graphene substrate. The k^0 obtained using α = 0.5 is in good agreement with literature (discussed later), indicating the assumption is reasonable. It should be noted that an anomalous α value on graphene electrode has been reported, the reason for which remains an open question.[5] The simulated feedback curves with different values of k^0 can be seen in Supporting Information Figure S9. By fitting the current feedback curves, k^0 was obtained for each defective graphene pattern. The pristine graphene is found to have a k^0 of $(1.0 \pm 0.2) \times 10^{-2}$ cm/s (region A in Figure 2a). This value is a little lower than reported values from 2×10^{-2} to 4.2×10^{-2} cm/s for pristine CVD graphene in aqueous solution.[1,5] The difference can be attributed to the variation in the intrinsic quality of the sample. As can be observed in the AFM images (Supporting Information Figure S10), the morphology of the pristine graphene used in this work is uniform and smooth. In the work of ref 1, some disordered structures such as wrinkles and particulates could be observed, which likely account for higher electron transfer kinetics, as demonstrated in this study. Exposing the graphene and PMMA to electron beam or Ar^+

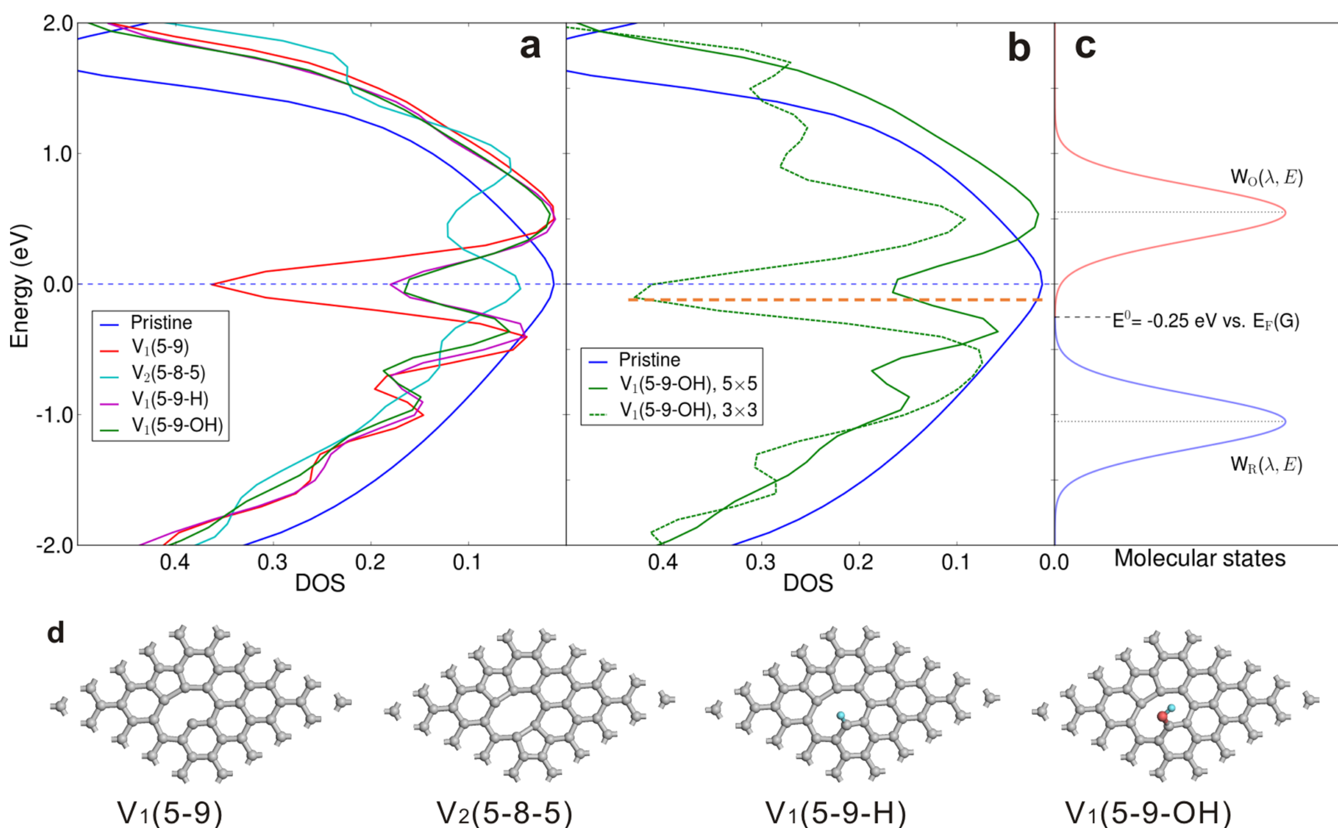

Figure 4. (a) Simulated DOS of the pristine graphene and graphene with different point vacancy defects (all in a 5 × 5 supercell to keep the same defect density), including reconstructed monovacancy V_1(5-9), reconstructed divacancy V_2(5-8-5), monovacancy incorporated with hydrogen V_1(5-9-H), and hydroxyl V_1(5-9-OH) groups. (b) Simulated DOS of graphene with different defect densities, from one V_1(5-9-OH) defect in a 5 × 5 supercell (50 carbon atoms) to a 3 × 3 supercell (18 carbon atoms). The latter case has a higher defect density and a higher DOS peak (dashed green line). (c) The density distribution of the reduced ($W_R(\lambda,E)$) and oxidized ($W_O(\lambda,E)$) states of FcMeOH. (d) Supercell structure of the four types of vacancy defects for simulation. Gray, carbon; red, oxygen; cyan, hydrogen.

irradiation is not likely to produce adsorbed electrochemically active species.[5,51] Furthermore, the samples have been annealed in the hydrogen atmosphere and are free of residuals and impurities, as evidenced by the Raman, AFM, and XPS results (discussed later).

Defect Density Correlated HET Rate of Single Layer Graphene and Theoretical Considerations. Figure 3d and e shows k^0 as a function of defect density (n_D) and L_D, respectively. The data points in red are from the measurement on the same single layer graphene sheet with three sets of patterns, as shown in Figure 2, Supporting Information Figure S6a and S6b. The detailed kinetic results are summarized in Table 1. A three-stage behavior can be observed from Figure 3d and e. First, the k^0 is slightly increased from $(1.0 \pm 0.2) \times 10^{-2}$ cm/s (pristine graphene) to $(4.0 \pm 0.5) \times 10^{-2}$ cm/s at a defect density of about $3.30 \times 10^{11}/\text{cm}^2$ (Figure 3d), corresponding to a L_D of about 10 nm (Figure 3e). The HET rate (k_{ET}) between graphene and FcMeOH can be described by the Gerischer–Marcus model in eqs 2 and 3.[52,53]

$$k_{ET} = \nu_n \int \varepsilon_{red}(E) f(E) DOS_G(E) W_O(\lambda, E)\, dE \quad (2)$$

$$W_O(\lambda, E) = \frac{1}{\sqrt{4\pi\lambda kT}} \exp\left(-\frac{(E - (E^0 + \lambda))^2}{4\lambda kT}\right) \quad (3)$$

where ν_n is the nuclear frequency factor, $\varepsilon_{red}(E)$ is the proportionality function, $f(E)$ is the Fermi function, DOS_G is the DOS of graphene, $W_O(\lambda,E)$ is the probability density function of the oxidized (unoccupied) states of FcMeOH in solution, and λ is the reorganization energy of FcMeOH. The electron transfer kinetics is determined by the integration of the number of electronic states of graphene and the number of oxidized states of FcMeOH near the Fermi level (for a reduction reaction).[23,54,55]

The improved HET rate can be understood by the increase of DOS near the Dirac point in defective graphene.[35] Figure 4a and b shows the DOS of the pristine and defective graphene. Figure 4c presents the density distribution of the electronic states of FcMeOH, where the light red peak represents the oxidized state and the light blue peak represents the reduced (occupied) state ($W_R(\lambda,E)$). The energy level in Figure 4 is aligned with respect to the Dirac point (Fermi level of undoped pristine graphene, the horizontal dashed line in Figure 4a and b, see Supporting Information section S4). FcMeOH is a quasi-reversible redox with fast HET rate. When a relatively large overpotential is applied on the substrate, the approach curves for different k^0 are close to those obtained under the diffusion-limited condition. Thus, the substrate kinetics cannot be distinguished apparently. Nevertheless, the approach curves obtained under a weak polarization condition have significant differences for and better discrimination of different substrate kinetics (k^0).[53] Therefore, the electrode potential applied is slightly more negative (i.e., higher energy, indicated by the orange dashed line in Figure 4b) than the standard redox potential (E^0) of FcMeOH, to provide a weak polarization

condition. The DOS of the pristine graphene (solid blue lines in Figure 4a and b) is insufficient near this energy, which hampers its electrochemical activity.

With the introduction of point vacancy defects, the defect induced midgap states with high DOS are observed near the Dirac point (Figure 4a and b).[35] The four possible types of vacancy defects simulated (Supporting Information section S5) all show the midgap states (Figure 4a). Their supercell structures are shown in Figure 4d. In comparison with pristine graphene, the defective graphene provides higher DOS that enlarge the overlap between the electronic states of graphene and FcMeOH, which facilitates HET from graphene to FcMeOH (reduction).

The midgap states induced by the point defect are spatially localized around the defects.[35] Two length scales should be considered. The first one is the radius of the structurally disordered area, caused directly by the ion irradiation, which was observed to be about 1 nm (shown as the red colored area in Figure 3a−c).[36] The second one is the distance in which the DOS decays to zero, which is about 3 nm.[35,56] The graphene area within the radius of 3 nm is thus more active because of the higher DOS than pristine graphene. Hence, the graphene in the outer area (1 nm < r < 3 nm) is electronically activated but remains pristine structure of graphene (shown as yellow colored area in Figure 3a−c). In the case of low defect density, the defects are independent and far from each other. Therefore, the graphene is partially activated, while the remaining area remains pristine (not activated), as seen in Figure 3a. With the defect density increasing, the activated area of defects starts to coalesce and the graphene becomes fully activated when L_D reaches 6 nm (Figure 3b). Indeed, a significant enhancement of k^0 from $(1.0 \pm 0.2) \times 10^{-1}$ to $(5.0 \pm 1.0) \times 10^{-1}$ cm/s is observed in a relatively high defect density, ranging from $(8.89 \pm 0.87) \times 10^{11}$ to $(7.39 \pm 0.58) \times 10^{12}$/cm^2, corresponding to L_D from 6.00 ± 0.29 to 2.10 ± 0.10 nm, respectively.

A correlation between the HET rate and the local DOS has been observed previously on a diamond electrode.[57] As seen in Figure 4b, increasing the defect density can lead to a higher DOS (from solid to dashed green line) that will lead to a faster kinetics. In this moderate defect density range, single layer graphene becomes much more activated and leads to higher k^0 as observed.

The above results suggest that a certain defect density is necessary for better electrochemical performance, especially for electrocatalytic reactions where defects act generally as active sites for adsorption and reactions.[7] However, the electron transport capability (conductivity) within the bulk single layer graphene sheet should be considered, which is vital to ensure a fast HET rate. The carrier mobility of pristine graphene is extremely high even under ambient conditions.[58] However, defects can scatter carriers that results in reduction of the conductivity.[59−61] For instance, the resistance of single-wall carbon nanotube increases by 3 orders of magnitude with only 0.03% level of divacancies.[32] Good conductivity is essential especially when graphene is to be functionalized in electrochemical or electronic devices. As seen in Figure 3d and e, the k^0 decreases dramatically from $(5.0 \pm 1.0) \times 10^{-1}$ to $(4.0 \pm 0.5) \times 10^{-2}$ cm/s at a defect density of $(8.34 \pm 0.64) \times 10^{12}$/cm^2 ($L_D = 1.96 \pm 0.08$ nm). In a microscopic view, L_D less than 2 nm means that the structurally disordered area starts to coalesce. Consequently, electrons will be highly scattered and the conductivity drops remarkably due to the loss of the perfect sp^2 lattice, which supports the electron transport in the basal plane. Note that $k^0 = 4.0 \times 10^{-2}$ cm/s is still higher than that of the pristine graphene, indicating that graphene is still activated. However, the decrease in conductivity starts to dominate the overall performance. This effect would account for the decrease of k^0 in the high defect density range.

Further increasing the defect density to higher than $(1.02 \pm 0.06) \times 10^{13}$/cm^2 results in $k^0 < (2.0 \pm 0.5) \times 10^{-3}$ cm/s. In fact, the approaching curve shows an insulating behavior (Figure 2d, curve H). Note that the highest defect density in this study is still lower than that of the fully disordered graphene, which has a defect density of 10^{15}/cm^2 (i.e., one defect per four carbon atoms).[62] Thus, by balancing the amount of defect sites with good conductivity, the optimal electrochemical activity of single layer graphene should be figured out. It is impressive that $k^0 = (5.0 \pm 1.0) \times 10^{-1}$ cm/s, 50-fold faster than that of the pristine graphene, is observed at the defect density of $(7.39 \pm 0.58) \times 10^{12}$/cm^2 ($L_D = 2.10 \pm 0.10$ nm). A L_D of 2.10 nm corresponds to a defect density when all of the carbon atoms in graphene are activated, but the single layer graphene sheet still maintains its sp^2 network. This is a critical state before the graphene becomes structurally destroyed. Figure 3d and e also includes the results obtained from another single layer graphene sheet (the data points in green), the Raman and SECM results of which are shown in Supporting Information Figure S6c and S6d. These data follow the same trend of defect density dependence. The above results suggest a clear correlation between defect density and electrochemical activity of single layer graphene. A precise control of the defect density is essential to optimize the electrochemical performance. Although the remarkable electrochemical properties of the defects or edge plane sites have long been recognized for graphite and recently for graphene electrodes, our findings show an exciting approach to make use of point defects in tailoring the electrochemical properties of single layer graphene.

Additionally, the defects are quite stable. Supporting Information Figure S11 shows the Raman spectra before and after the electrochemical measurements (and stored under the ambient condition for 6 months). The relative intensity and the bandwidth of all of the Raman bands remain unchanged, suggesting excellent structural stability of the defects. XPS results indicate that the vacancy defects are incorporated with the −OH groups (Supporting Information Figure S12), which were found to be thermodynamically stable and survived even after being annealed at 1000 °C.[63,64] Note that the outer-sphere electrochemical processes of FcMeOH are not sensitive to the surface oxygen groups. Therefore, the −OH groups may help to stabilize the defects by bonding to the under-coordinated carbon atoms (see Supporting Information section S6 for further discussion).

As noted above, Raman spectroscopy is very sensitive to the electronic structure of graphene. Furthermore, there is a good correlation between the Raman mapping and SECM imaging results. Thus, it is reasonable that the electrochemical activity of single layer graphene may be predicted simply by Raman spectroscopy. Upon closer examination of the Raman spectra of graphene (Figure 2 and Supporting Information Figure S6), it is instructive to reveal that different Raman features correspond to different electrochemical activity stages. For graphene with high activity, the D band is much stronger than the G band, and the D′ and 2D peaks can still be resolved (Figure 2c, spectra E and F, see also Supporting Information Figure S6). These features indicate not only the high defect density, but also the

integrity of the sp^2 graphene sheet. When the activity of graphene decreases, the G and D′ peaks are totally merged, the 2D peak becomes invisible, and all of the Raman peaks become broad (Figure 2c, spectra G and H; see also Supporting Information Figure S6). These features may indicate that the graphene is damaged in a structure of highly disordered sp^2 network, which results in a decreased conductivity. Therefore, Raman (mapping) spectroscopy may serve as a fast and nondestructive method to screen the electrochemical activity of single layer graphene. Further study is needed to address this issue.

4. CONCLUSION

In summary, we have demonstrated that the electrochemical activity of single layer graphene depends strongly on its defect density. In the low defect density range, the graphene is partially activated and the HET rate is slightly enhanced. At very high defect density range, the scattering of the electrons leads to the reduction of the conductivity, thus resulting in lower (but still enhanced) HET rate. A moderate defect density range is necessary for optimal electrochemical activity. By balancing the defect induced increase of DOS and decrease of conductivity of single layer graphene, the optimal HET rate constant of $k^0 = (5.0 \pm 1.0) \times 10^{-1}$ cm/s is achieved at a defect density of $(7.39 \pm 0.58) \times 10^{12}/\text{cm}^2$, corresponding to a mean distance between defects (L_D) of 2.10 ± 0.10 nm. That is about 50-fold faster than that of the pristine graphene ($k^0 = (1.0 \pm 0.2) \times 10^{-2}$ cm/s). This defect density is a critical value, at which the whole single layer graphene sheet becomes electronically activated while maintaining the sp^2 network. The quantitative correlation between defect density and electrochemical activity provides new insights into the optimization of graphene-based electrochemical devices from electrocatalysis to energy conversion and storage. The introduction of point defects in the basal plane of single layer graphene also allows the full activation of carbon atoms in graphene. The patterned graphene with various defect densities may be useful to spatially control chemical reactions. Furthermore, we provide a method to tailor single layer graphene and other ultrathin two-dimensional materials through defect density engineering.

■ ASSOCIATED CONTENT

Supporting Information

Additional Raman and SECM results, AFM, XPS, and electrochemical characterization results, and further discussion. This material is available free of charge via the Internet at http://pubs.acs.org.

■ AUTHOR INFORMATION

Corresponding Authors

dpzhan@xmu.edu.cn

bren@xmu.edu.cn

Author Contributions

[§]J.-H.Z. and J.Z. contributed equally.

Notes

The authors declare no competing financial interest.

■ ACKNOWLEDGMENTS

We thank Dr. Yanping Zheng for help with the XPS measurements and Teng-Xiang Huang for help with the AFM measurements. We thank Prof. Christopher T. Williams for help with the writing and his comments. We thank Dr. Liu-Bin Zhao and Prof. Shanshan Chen for their fruitful discussions. We acknowledge the support from the MOST (2013CB933703, 2012CB932902, and 2011YQ03012400), NSFC (21227004, 21321062, J1310024, and 21061120456), and MOE (IRT13036) programs.

■ REFERENCES

(1) Li, W.; Tan, C.; Lowe, M. A.; Abruña, H. D.; Ralph, D. C. *ACS Nano* **2011**, *5*, 2264.
(2) Valota, A. T.; Kinloch, I. A.; Novoselov, K. S.; Casiraghi, C.; Eckmann, A.; Hill, E. W.; Dryfe, R. A. W. *ACS Nano* **2011**, *5*, 8809.
(3) Zhong, J.-H.; Liu, J.-Y.; Li, Q.; Li, M.-G.; Zeng, Z.-C.; Hu, S.; Wu, D.-Y.; Cai, W.; Ren, B. *Electrochim. Acta* **2013**, *110*, 754.
(4) Toth, P. S.; Valota, A. T.; Velicky, M.; Kinloch, I. A.; Novoselov, K. S.; Hill, E. W.; Dryfe, R. A. W. *Chem. Sci.* **2014**, *5*, 582.
(5) Ritzert, N. L.; Rodríguez-López, J.; Tan, C.; Abruña, H. D. *Langmuir* **2013**, *29*, 1683.
(6) Ji, H.; Zhao, X.; Qiao, Z.; Jung, J.; Zhu, Y.; Lu, Y.; Zhang, L. L.; MacDonald, A. H.; Ruoff, R. S. *Nat. Commun.* **2014**, *5*, 3317.
(7) Li, Y.; Zhou, W.; Wang, H.; Xie, L.; Liang, Y.; Wei, F.; Idrobo, J. C.; Pennycook, S. J.; Dai, H. *Nat. Nanotechnol.* **2012**, *7*, 394.
(8) Jiao, Y.; Zheng, Y.; Jaroniec, M.; Qiao, S. Z. *J. Am. Chem. Soc.* **2014**, *136*, 4394.
(9) Zheng, Y.; Jiao, Y.; Zhu, Y.; Li, L. H.; Han, Y.; Chen, Y.; Du, A.; Jaroniec, M.; Qiao, S. Z. *Nat. Commun.* **2014**, *5*, 3783.
(10) Yan, L.; Zheng, Y. B.; Zhao, F.; Li, S. J.; Gao, X. F.; Xu, B. Q.; Weiss, P. S.; Zhao, Y. L. *Chem. Soc. Rev.* **2012**, *41*, 97.
(11) Georgakilas, V.; Otyepka, M.; Bourlinos, A. B.; Chandra, V.; Kim, N.; Kemp, K. C.; Hobza, P.; Zboril, R.; Kim, K. S. *Chem. Rev.* **2012**, *112*, 6156.
(12) Banhart, F.; Kotakoski, J.; Krasheninnikov, A. V. *ACS Nano* **2010**, *5*, 26.
(13) Zandiatashbar, A.; Lee, G. H.; An, S. J.; Lee, S.; Mathew, N.; Terrones, M.; Hayashi, T.; Picu, C. R.; Hone, J.; Koratkar, N. *Nat. Commun.* **2014**, *5*, 3186.
(14) Tapasztó, L.; Dobrik, G.; Nemes-Incze, P.; Vertesy, G.; Lambin, P.; Biró, L. P. *Phys. Rev. B* **2008**, *78*, 233407.
(15) Yazyev, O. V. *Phys. Rev. Lett.* **2008**, *101*, 037203.
(16) Zhou, W.; Lee, J.; Nanda, J.; Pantelides, S. T.; Pennycook, S. J.; Idrobo, J. C. *Nat. Nanotechnol.* **2012**, *7*, 161.
(17) Bowling, R. J.; Packard, R. T.; McCreery, R. L. *J. Am. Chem. Soc.* **1989**, *111*, 1217.
(18) Rice, R. J.; McCreery, R. L. *Anal. Chem.* **1989**, *61*, 1637.
(19) Robinson, R. S.; Sternitzke, K.; McDermott, M. T.; McCreery, R. L. *J. Electrochem. Soc.* **1991**, *138*, 2412.
(20) Banks, C. E.; Davies, T. J.; Wildgoose, G. G.; Compton, R. G. *Chem. Commun.* **2005**, 829.
(21) Davies, T. J.; Hyde, M. E.; Compton, R. G. *Angew. Chem., Int. Ed.* **2005**, *44*, 5121.
(22) Ambrosi, A.; Sasaki, T.; Pumera, M. *Chem.—Asian J.* **2010**, *5*, 266.
(23) McCreery, R. L. *Chem. Rev.* **2008**, *108*, 2646.
(24) Brownson, D. A. C.; Kampouris, D. K.; Banks, C. E. *Chem. Soc. Rev.* **2012**, *41*, 6944.
(25) Lai, S. C. S.; Patel, A. N.; McKelvey, K.; Unwin, P. R. *Angew. Chem., Int. Ed.* **2012**, *51*, 5405.
(26) Patel, A. N.; Collignon, M. G.; O'Connell, M. A.; Hung, W. O.; McKelvey, K.; Macpherson, J. V.; Unwin, P. R. *J. Am. Chem. Soc.* **2012**, *134*, 20117.
(27) Güell, A. G.; Ebejer, N.; Snowden, M. E.; McKelvey, K.; Macpherson, J. V.; Unwin, P. R. *Proc. Natl. Acad. Sci. U.S.A.* **2012**, *109*, 11487.
(28) Tan, C.; Rodríguez-López, J.; Parks, J. J.; Ritzert, N. L.; Ralph, D. C.; Abruña, H. D. *ACS Nano* **2012**, *6*, 3070.
(29) Brownson, D. A. C.; Banks, C. E. *Phys. Chem. Chem. Phys.* **2011**, *13*, 15825.

(30) Yuan, W.; Zhou, Y.; Li, Y.; Li, C.; Peng, H.; Zhang, J.; Liu, Z.; Dai, L.; Shi, G. *Sci. Rep.* **2013**, *3*, 2248.
(31) Zhang, B.; Fan, L.; Zhong, H.; Liu, Y.; Chen, S. *J. Am. Chem. Soc.* **2013**, *135*, 10073.
(32) Gómez-Navarro, C.; de Pablo, P. J.; Gómez-Herrero, J.; Biel, B.; Garcia-Vidal, F. J.; Rubio, A.; Flores, F. *Nat. Mater.* **2005**, *4*, 534.
(33) Krasheninnikov, A. V.; Banhart, F. *Nat. Mater.* **2007**, *6*, 723.
(34) Palacios, J. J.; Fernández-Rossier, J.; Brey, L. *Phys. Rev. B* **2008**, *77*, 195428.
(35) Ugeda, M. M.; Brihuega, I.; Guinea, F.; Gómez-Rodríguez, J. M. *Phys. Rev. Lett.* **2010**, *104*, 096804.
(36) Lucchese, M. M.; Stavale, F.; Ferreira, E. H. M.; Vilani, C.; Moutinho, M. V. O.; Capaz, R. B.; Achete, C. A.; Jorio, A. *Carbon* **2010**, *48*, 1592.
(37) Cançado, L. G.; Jorio, A.; Ferreira, E. H.; Stavale, F.; Achete, C. A.; Capaz, R. B.; Moutinho, M. V.; Lombardo, A.; Kulmala, T. S.; Ferrari, A. C. *Nano Lett.* **2011**, *11*, 3190.
(38) Eckmann, A.; Felten, A.; Verzhbitskiy, I.; Davey, R.; Casiraghi, C. *Phys. Rev. B* **2013**, *88*, 035426.
(39) Dresselhaus, M. S.; Jorio, A.; Saito, R. *Annu. Rev. Condens. Matter Phys.* **2010**, *1*, 89.
(40) Ferrari, A. C.; Basko, D. M. *Nat. Nanotechnol.* **2013**, *8*, 235.
(41) Chen, S.; Ji, H.; Chou, H.; Li, Q.; Li, H.; Suk, J. W.; Piner, R.; Liao, L.; Cai, W.; Ruoff, R. S. *Adv. Mater.* **2013**, *25*, 2062.
(42) Liang, X.; Sperling, B. A.; Calizo, I.; Cheng, G.; Hacker, C. A.; Zhang, Q.; Obeng, Y.; Yan, K.; Peng, H.; Li, Q.; Zhu, X.; Yuan, H.; Hight Walker, A. R.; Liu, Z.; Peng, L.; Richter, C. A. *ACS Nano* **2011**, *5*, 9144.
(43) Perdew, J. P.; Burke, K.; Ernzerhof, M. *Phys. Rev. Lett.* **1996**, *77*, 3865.
(44) Giannozzi, P.; Baroni, S.; Bonini, N.; Calandra, M.; Car, R.; Cavazzoni, C.; Ceresoli, D.; Chiarotti, G. L.; Cococcioni, M.; Dabo, I.; Dal Corso, A.; de Gironcoli, S.; Fabris, S.; Fratesi, G.; Gebauer, R.; Gerstmann, U.; Gougoussis, C.; Kokalj, A.; Lazzeri, M.; Martin-Samos, L.; Marzari, N.; Mauri, F.; Mazzarello, R.; Paolini, S.; Pasquarello, A.; Paulatto, L.; Sbraccia, C.; Scandolo, S.; Sclauzero, G.; Seitsonen, A. P.; Smogunov, A.; Umari, P.; Wentzcovitch, R. M. *J. Phys.: Condens. Matter* **2009**, *21*, 395502.
(45) Blöchl, P. E. *Phys. Rev. B* **1994**, *50*, 17953.
(46) Monkhorst, H. J.; Pack, J. D. *Phys. Rev. B* **1976**, *13*, 5188.
(47) Lehtinen, O.; Kotakoski, J.; Krasheninnikov, A. V.; Tolvanen, A.; Nordlund, K.; Keinonen, J. *Phys. Rev. B* **2010**, *81*, 153401.
(48) Ugeda, M. M.; Fernandez-Torre, D.; Brihuega, I.; Pou, P.; Martinez-Galera, A. J.; Perez, R.; Gomez-Rodriguez, J. M. *Phys. Rev. Lett.* **2011**, *107*, 116803.
(49) Ferrari, A. C.; Robertson, J. *Phys. Rev. B* **2000**, *61*, 14095.
(50) Eckmann, A.; Felten, A.; Mishchenko, A.; Britnell, L.; Krupke, R.; Novoselov, K. S.; Casiraghi, C. *Nano Lett.* **2012**, *12*, 3925.
(51) Brownson, D. A. C.; Metters, J. P.; Kampouris, D. K.; Banks, C. E. *Electroanalysis* **2011**, *23*, 894.
(52) Gerischer, H. In *Physical Chemistry: An Advanced Treatise*; Eyring, H., Henderson, D., Jost, W., Eds.; Academic Press, Inc.: New York, 1970; Vol. *9A*.
(53) Bard, A. J.; Faulkner, L. R. *Electrochemical Methods, Fundamentals and Applications*, 2nd ed.; John Wiley and Sons: New York, 2001.
(54) Heller, I.; Kong, J.; Williams, K. A.; Dekker, C.; Lemay, S. G. *J. Am. Chem. Soc.* **2006**, *128*, 7353.
(55) McCreery, R. L.; McDermott, M. T. *Anal. Chem.* **2012**, *84*, 2602.
(56) Ruffieux, P.; Melle-Franco, M.; Gröning, O.; Bielmann, M.; Zerbetto, F.; Gröning, P. *Phys. Rev. B* **2005**, *71*, 153403.
(57) Patten, H. V.; Meadows, K. E.; Hutton, L. A.; Iacobini, J. G.; Battistel, D.; McKelvey, K.; Colburn, A. W.; Newton, M. E.; Macpherson, J. V.; Unwin, P. R. *Angew. Chem., Int. Ed.* **2012**, *51*, 7002.
(58) Geim, A. K.; Novoselov, K. S. *Nat. Mater.* **2007**, *6*, 183.
(59) Chen, J.-H.; Cullen, W. G.; Jang, C.; Fuhrer, M. S.; Williams, E. D. *Phys. Rev. Lett.* **2009**, *102*, 236805.
(60) Lherbier, A.; Dubois, S. M.; Declerck, X.; Roche, S.; Niquet, Y. M.; Charlier, J. C. *Phys. Rev. Lett.* **2011**, *106*, 046803.
(61) Hwang, J. Y.; Kuo, C. C.; Chen, L. C.; Chen, K. H. *Nanotechnology* **2010**, *21*, 465705.
(62) Jorio, A.; Lucchese, M. M.; Stavale, F.; Ferreira, E. H.; Moutinho, M. V.; Capaz, R. B.; Achete, C. A. *J. Phys.: Condens. Matter* **2010**, *22*, 334204.
(63) Boukhvalov, D. W.; Katsnelson, M. I. *J. Am. Chem. Soc.* **2008**, *130*, 10697.
(64) Ganguly, A.; Sharma, S.; Papakonstantinou, P.; Hamilton, J. *J. Phys. Chem. C* **2011**, *115*, 17009.